Investigation of the (1 0 0) and (0 0 1) surfaces of the Al5Fe2 intermetallic compound

L Boulley, D. Kandaskalov, M-C de Weerd, S. Migot, J. Ghanbaja, S Šturm, Pascal Boulet, J. Ledieu, E. Gaudry, V Fournée

▶ **To cite this version:**

L Boulley, D. Kandaskalov, M-C de Weerd, S. Migot, J. Ghanbaja, et al.. Investigation of the (1 0 0) and (0 0 1) surfaces of the Al5Fe2 intermetallic compound. Applied Surface Science, 2021, 542, pp.148540. 10.1016/j.apsusc.2020.148540 . hal-03043810

HAL Id: hal-03043810
https://hal.science/hal-03043810

Submitted on 26 Oct 2021

HAL is a multi-disciplinary open access archive for the deposit and dissemination of scientific research documents, whether they are published or not. The documents may come from teaching and research institutions in France or abroad, or from public or private research centers.

L'archive ouverte pluridisciplinaire **HAL**, est destinée au dépôt et à la diffusion de documents scientifiques de niveau recherche, publiés ou non, émanant des établissements d'enseignement et de recherche français ou étrangers, des laboratoires publics ou privés.

Investigation of the (100) and (001) surfaces of the Al_5Fe_2 intermetallic compound

June 4, 2021

L. Boulley[a,c], D. Kandaskalov[a,c], M.-C. de Weerd[a,c], S. Migot[a,c], J. Ghanbaja[a,c], S. Sturm[b,c], P. Boulet[a,c], J. Ledieu[a,c], É. Gaudry[a,c,1], V. Fournée[a,c,2]

[a] Institut Jean Lamour (UMR 7198 CNRS-Nancy-Université de Lorraine), Campus ARTEM - 2 allée André Guinier, F-54011 Nancy, France

[b] Jožef Stefan Institute, Department for Nanostructured Materials, Jamova cesta 39, SI-1000 Ljubljana, Slovenia

[c] International Associated Laboratory PACS2, CNRS Université de Lorraine, Nancy, France and Jožef Stefan Institute, Ljubljana, Slovenia

Abstract

The bulk structure of the η-Al_5Fe_2 intermetallic compound consists in an ordered framework of pentagonal antiprims with composition Al_2Fe inside which nearly continuous chains of fractionally occupied Al sites exist. At low temperature, ordering of these Al channel atoms can occur, leading to various superstructures. Although the Al_5Fe_2 intermetallic phase is of technological importance being present in protective coating for steel parts, a detailed surface investigation of this compound has not been reported yet. Here we describe the growth of a single crystal of the Al_5Fe_2 compound by the Czochralski method. Its bulk structure is identified as the low temperature polymorph η". Density Functional Theory calculations were performed to determine its formation enthalpy and its electronic structure. A deep pseudogap is noticeable at the Fermi energy, and this compound is found to be magnetic. Two samples have been extracted, presenting a surface oriented either perpendicular to the channel's direction ((001) surface) or parallel to them ((100) surface). The two surfaces have been investigated by x-ray photoemission spectroscopy, low-energy electron diffraction and scanning tunneling microscopy. Both surfaces exhibit some superstructures of various complexities, whose origin can be explained in the light of density functional theory calculations performed on model surfaces.

[1]Corresponding author. e-mail: emilie.gaudry@univ-lorraine.fr

[2]Corresponding author. e-mail: vincent.fournee@univ-lorraine.fr

1 Introduction

Structurally complex intermetallics can be found in many transition metal aluminides, sometimes exhibiting long-range quasiperiodic order or being large unit cell periodic approximants. The Al_5Fe_2 intermetallic phase is one such compound. It is considered as a low order approximant of Al-based decagonal phases because its structure contains pseudo-decagonal columnar motifs. It is also a technologically important compound used to protect steel against corrosion and oxidation. The Al_5Fe_2 easily forms through Al diffusion into steel during aluminum pack cementation or hot dipping of steel parts into molten Al bath, resulting in a thick protective coating of the intermetallic phase [1, 2].

The η-Al_5Fe_2 compound forms congruently at 1442 K and has an approximate solubility range between 70 and 73 at.% [3, 4, 5, 6]. The structure of this phase was first reported by Schubert *et al.* in 1953 (space group *Cmcm*, a = 7.66 Å, b = 6.39 Å and c = 4.19 Å) [7]. The unit cell geometry was confirmed later by Ellner *et al.* in a study of liquid-quenched Al_5Fe_2 samples [8]. They also concluded to the *Cmcm* space group based on powder diffraction patterns. However, unexpected split satellite reflections were also observed in electron diffraction patterns *(0kl)* and *(h,h+2l,l)*. These reflections did not conform to the *Cmcm* space group. They could be indexed by *(0,k,1/2)* (not considering their splitting), which would correspond to a doubling of the lattice parameter c. The structure was later refined by Burkhardt *et al.* based on single-crystal x-ray diffraction experiment, also in the *Cmcm* (#63) space group, with lattice parameters a = 7.6559 Å, b = 6.4154 Å and c = 4.2184 Å[9]. The atomic structure was described by a rigid framework of pentagonal antiprisms extending along the [001] direction and connected by side edges (Fig. 1a). These channels are formed by fully occupied Fe (4c) and Al1 (8g) sites. Additional partially occupied Al sites form a disordered chain confined within the channels. Burkhardt *et al.* proposed to describe the Al chains by Al2 (4a) and Al3 (8f) sites with site occupation factors of 0.36 and 0.23 respectively, leading to a $Al_{5.6}Fe_2$ phase, i.e. in excess of Al (73.7 at.%) with respect to the solubility range specified in [3]. Additional strip-like diffuse reflections were also observed in Weissenberg photographs of the *(h,h+2l,l)* projection with non-integer indices l=3/2 and l=5/2, consistent with Ellner's electron diffraction patterns. These additional reflections were ascribed to the partially disordered Al chains in the channels along c direction and were not considered further. A later report by Stein *et al.* only differs by the Al distribution along the channels [10]. They propose to describe the channels by Al2 (8f) and Al3 (4a) sites with both site occupation factors equal to 0.167. The stoechiometry is then Al_5Fe_2 (71.4 at.% of Al).

More recently, several structural polymorphs of the η phase were re-

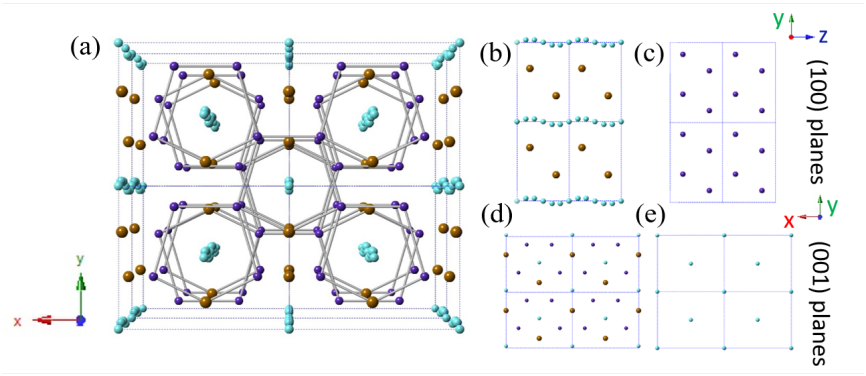

Figure 1: (a) 3D perspective view of the Al_5Fe_2 crystal structure along the c direction according to the model of Burkhardt *et al.* [9]. Brown spheres denote Fe atoms, purple spheres represent Al1 atoms and closely spaced cyan spheres are Al2 and Al3 atom sites in the channels with partial occupancies. The bonds illustrate the 3D framework of pentagonal antiprisms formed by Fe and Al1 atoms. (b,c) and (d,e) show possible bulk truncated (100) and ((001) planes, respectively.

ported. A new crystal structure η'-Al_8Fe_3 has been identified and interpreted as a low temperature phase of the disordered η phase [5, 6]. It has a tripled superlattice structure based on the orthorhombic lattice, in which Al atoms occupy two ninths of the partially occupied (Al2 and Al3) channel sites in an ordered manner, leading to a monoclinic space group *C2/c* and a Al_8Fe_3 composition (72.7 at.% of Al). Two additional low temperature phases have also been identified for more Fe-rich compositions, exhibiting long-range order of the channel atoms. Reported structural resolutions of these phases suggested that the channel atomic positions might be occupied not only by Al but also partially with Fe atoms. The structure of these phases, termed η" and η"', were interpreted either as incommensurately modulated composite crystals [11] or as commensurate long-period ordered superlattice structures based on the parent orthorhombic Al_5Fe_2 unit cell [12]. All these low temperature phases correspond to slightly different chemical compositions and are obtained by annealing crystals in a temperature range between 250 and 400 °C.

The stability of Al_5Fe_2 was further investigated using first-principles total energy calculations by Mihalkovič *et al.* [13]. It required an optimization of the arrangements of the partially occupied Al2 and Al3 channel sites. After exploring various configurations, they found an energetically optimized structure that contains four Al atoms in three c repeat units per channel.

However the structure is slightly unstable at 0 K according to these first-principle calculations, which instead predict stability of another (hypothetical) structure based on the prototype $MoSi_2$ structure, that is not observed experimentally. Alternate structure placing five Al atoms in four c repeat units per channel exhibits a deep pseudogap in the electron density of states at the Fermi energy but the overall energy increased by 4 meV/atom. It was concluded that the Al_5Fe_2 compounds is stabilized at high temperature by their vibrational entropy arising from Al diffusion through the channels. A similar study was reported by Sakidja *et al.* exploring the stability of the compound as a function of the partial occupation of Al vacancy sites, concluding that a certain level of excess Al relative to the stoechiometric concentration may contribute to lower the total energy of the system [14]. According to Vinokur *et al.*, the Al excess is linked to the requirement from the Fe bonding network to fulfill the (18-n) electron rule, leading to an optimized electronic structure for which the Fermi level falls at the center of a deep pseudogap [15].

Here we report a study of two low-index surfaces of the Al_5Fe_2 compound. A large single crystal has been grown by the Czochralski method. The bulk structure has been investigated, experimentally by single crystal x-ray diffraction and transmission electron microscopy, and theoretically by Density Functional Theory (DFT) calculations. Superlattice reflections are ascribed to the low temperature polymorph η". Two samples have been extracted, presenting a surface oriented either perpendicular to the channel's direction (the (001) surface) or parallel to them (the (100) surface). The structural models of truncated (001) and (100) surfaces expected from the bulk Al_5Fe_2 are shown in Fig. 1(b-d). The two surfaces have been investigated by x-ray photoemission spectroscopy, low-energy electron diffraction and scanning tunneling microscopy. Both surfaces exhibit some superstructures of various complexities, whose origin can be explained in the light of DFT calculations performed on model surfaces. The next section describes the experimental and computational details. Then the results are presented and discussed for the two different surfaces before we conclude.

2 Methods

2.1 Experimental details

According to the phase diagram, the Al_5Fe_2 compound can be grown congruently [3]. An ingot with a nominal composition of $Al_{71.4}Fe_{28.6}$ was first prepared by induction melting of the pure elements (Al 4N, Fe 3N7, Alfa Aesar) under an Ar atmosphere. Then a single crystal was grown by the Czochralski method. The single crystal was pulled from the melted ingot with a constant growth rate of 1 mm/h. It had a diameter of up

to 15 mm and was several centimeter in length. The chemical composition measured by electron probe microanalysis (EPMA) was $Al_{72.2}Fe_{27.8}$. The single crystal was oriented by back-Laue scattering and two samples were extracted to present either a (001) or a (100) surface. The surfaces of the oriented slices were mechanically polished with diamond paste down to grain size 0.25 μm leading to a mirror-like appearance. Clean surfaces were prepared by repeated cycles of Ar^+ sputtering (2 kV) and annealing at various temperatures under ultra-high vacuum (UHV, base pressure 1.10^{-10} mbar). The annealing temperature was measured using an optical pyrometer with the emissivity set to 0.35. The structural quality and the cleanliness of the surface were checked by low-energy electron diffraction (LEED), X-ray photoemission spectroscopy (XPS, Mg Kα) and scanning tunneling microscopy (STM). STM images were recorded using a commercial Omicron VT-STM/AFM in constant current mode and processed using the WsXM software [16]. An electron-transparent lamellae was extracted from the single crystal by a focused ion beam scanning electron microscope (FIB-SEM; Helios NanoLab 600i, FEI, Eindhoven, The Netherlands). The experimental high-angle annular dark-field scanning transmission electron microscopy (HAADF-STEM) images and selected area electron diffraction (SAED) were recorded using a Cs-aberration-corrected probe (JEM-ARM 200CF; JEOL, Tokyo, Japan) operated at 200 keV, with a spatial resolution in STEM mode of 0.08 nm. The collection semiangle for the HAADF detector was set between 45–180 mrad.

2.2 Computational details

Electronic structure calculations were performed using the plane wave Vienna *ab initio* simulation package (VASP) [17, 18, 19, 20], using the projector-augmented wave (PAW) method [21, 22] and the spin-polarized generalized gradient approximation (GGA-PBE) [23, 24]. Eight valence electrons were explicitely treated for Fe ($4s^1 3d^7$) and three for Al ($3s^2 3p^1$). Total energies were minimized until the energy differences became less than 10^{-6} eV between two electronic cycles during the structural optimizations. Atomic structures were relaxed till the Hellmann-Feynman forces were as low as 0.02 eV/Å (bulk calculations) and 0.03 eV/Å (slab calculations). In a few cases (slab calculations), the previous criteria has been increased to 0.1 eV/Å (models $F_{4vac}^{Al,Fe}$, $F_{6vac}^{Al,Fe}$, ${}^{vac}P^{Al}$). They were plotted using the VESTA software [25].

Bulk and slab calculations were performed using a 400 eV energy cut-off. The Brillouin zones of the different systems were sampled with Γ-centered Monkhorst-Pack k-point meshes. More precisely, we used a 7×7×13 k-point grid for the Al_5Fe_2 bulk structure proposed by Burkhardt *et al.* [9] and a 1×9×7 k-point grid for the η" and η"' long-range ordered Al_5Fe_2 structures.

The Brillouin zones of the supercells used to model the $Al_5Fe_2(100)$ and $Al_5Fe_2(001)$ surfaces were sampled with a 5×7×1 and 11×13×1 k-point grid, respectively.

The projected Crystal Orbital Hamilton Population (pCOHP) approach, implemented in the LOBSTER code [26, 27, 28, 29] was employed to analyze the chemical bonding network in the Al_5Fe_2 bulk crystal. This method re-extract Hamilton-weighted populations from plane-wave electronic structure calculations to develop a tool analogous to the crystal orbital Hamilton population (COHP) method [27]. Within this method, the electrons wave functions are projected onto the atomic local basis used for the DFT calculations. The charge spilling, i.e. electrons which cannot be projected onto the local basis, was found equal to 2.6%.

The (001) and (100) surfaces have been modeled with symmetric and asymmetric slabs, respectively, separated by a void thickness (> 10Å). While the magnetization was found to be zero for the bulk compounds, in agreement with a previous investigation – Al-Fe compounds containing less than 33% Fe were identified as non magnetic [13], the magnetization is not negligible for slab calculations. Asymmetric slabs were then built with an Al-rich bottom layer to minimize the number of surface Fe atoms.

Relative surface energies ($\gamma_{(hk\ell)} - \gamma^{ref}_{(hk\ell)}$) were computed as a function of the chemical potentials (μ_{Al}, μ_{Fe}) and number of atoms (N_{Al}, N_{Fe}) in the slab [30]:

$$\gamma^{\sigma}_{(hk\ell)} - \gamma^{ref}_{(hk\ell)} = \frac{1}{A_{slab(hk\ell)}} \times \Big[\Big(E^{\sigma}_{slab(hk\ell)}(N_{Al}, N_{Fe}) - E^{ref}_{slab(hk\ell)}(N^{ref}_{Al}, N^{ref}_{Fe}) \Big) - \mu_{Al}(N_{Al} - N^{ref}_{Al}) - \mu_{Fe}(N_{Fe} - N^{ref}_{Fe}) \Big] \quad (1)$$

In the previous equation, $E^{\sigma}_{slab(hk\ell)}$ is the total energy of the surface model with termination σ and $A_{slab(hk\ell)}$ is the area of the surface cell. The formation enthalpies of surface vacancies were calculated using:

$$\Delta H_f(\text{vac}) = E^{\sigma}_{slab(hk\ell)}(N_{Al}, N_{Fe}) - [E^{\sigma}_{slab(hk\ell)}(N_{Al}, N_{Fe} - 1) + \mu_{Fe}] \quad (2)$$

The chemical potentials of Al in fcc Al (μ^{bulk}_{Al}) and Fe in bcc Fe (μ^{bulk}_{Fe}) were taken as the cohesive energies of the elemental crystals (Tab. 1). The chemical potentials for Al and Fe in bulk Al_5Fe_2 were calculated through the Gibbs phase rule. Finally, the chemical potentials used in equation 1 were constrained in the range $\frac{7}{5}\Delta H_f \leq \mu_{Al} - \mu^{bulk}_{Al} \leq 0$. More precisely, the chemical potential of Fe in Al_5Fe_2 was taken as the cohesive energy of bcc Fe ($\mu_{Fe} = \mu^{bcc}_{Fe}$) in the Fe-rich limit, while $\mu_{Fe} = \frac{\Delta H_f}{2} + \mu^{bcc}_{Fe}$ in the Al-rich limit. Similarly, the chemical potential of Al in Al_5Fe_2 was taken as the cohesive energy of fcc Al ($\mu_{Al} = \mu^{fcc}_{Al}$) in the Al-rich limit, while $\mu_{Al} = \frac{\Delta H_f}{5} + \mu^{fcc}_{Al}$ in the Fe-rich limit.

		a (Å)	E_{coh} (eV)	Ref.
Al (fcc)	PBE	4.04	-3.52	
	PBE	4.04	-3.55	[31]
	exp.	4.05	-3.39	[32, 33]
Fe (bcc)	PBE	2.83	-4.86	
	PBE	2.83	-4.87	[34]
	exp.	2.93	-4.28	[35, 33]

Table 1: Cell parameters and cohesive energies for bulk Al and Fe.

3 Results and Discussion

3.1 Bulk structure of the Al_5Fe_2 crystal

A part of the single crystal has been crushed into powders and the X-ray diffraction pattern could be indexed as the orthorhombic η phase. However, single crystal X-ray diffraction revealed weaker reflections in addition to those main reflections from the η phase. This can be seen for example in the (0kl) precession map shown in Fig. 2(a). These additional reflections appear splitted along c*. A thin lamellae has been extracted by FIB from the (001)-oriented sample to observe the crystal structure using high-resolution transmission electron microscopy. The lamella is oriented perpendicular to the [100] axis. The corresponding selected area electron diffraction pattern is shown in Fig. 2(b).

Similar additional reflections are observed more clearly. They are located approximately at mid positions between the 000 and the 002 and 021 fundamental reflections and are splitted along c*. The split distance measured for spots at mid position between 000 and 021 fundamental spots is $\Delta^* \sim 0.086$ c*. A HAADF-STEM image of the structure is shown in Fig. 2(c) with [100] incidence and the corresponding projection of the crystal structure of the η phase according to the model by Burkhardt [9] is shown in Fig. 2(d). The images simply reveal the asymmetric dumbbell-shaped pattern arising from the Fe and Al1 positions with full occupancy forming the rigid framework of pentagonal antiprims. Other Al atoms at Al2 and Al3 partially occupied sites do not produce any clear contrast in these images. These results are consistent with previous observations reported in [11, 12] suggesting that our single crystal exhibits the structure of the low temperature polymorph η" arising from a long-range ordering of the channel atoms as mentioned in the Introduction. This is probably due to the temperature ramp after crystal pulling which must be slow enough to allow for the η to η" transformation upon cooling.

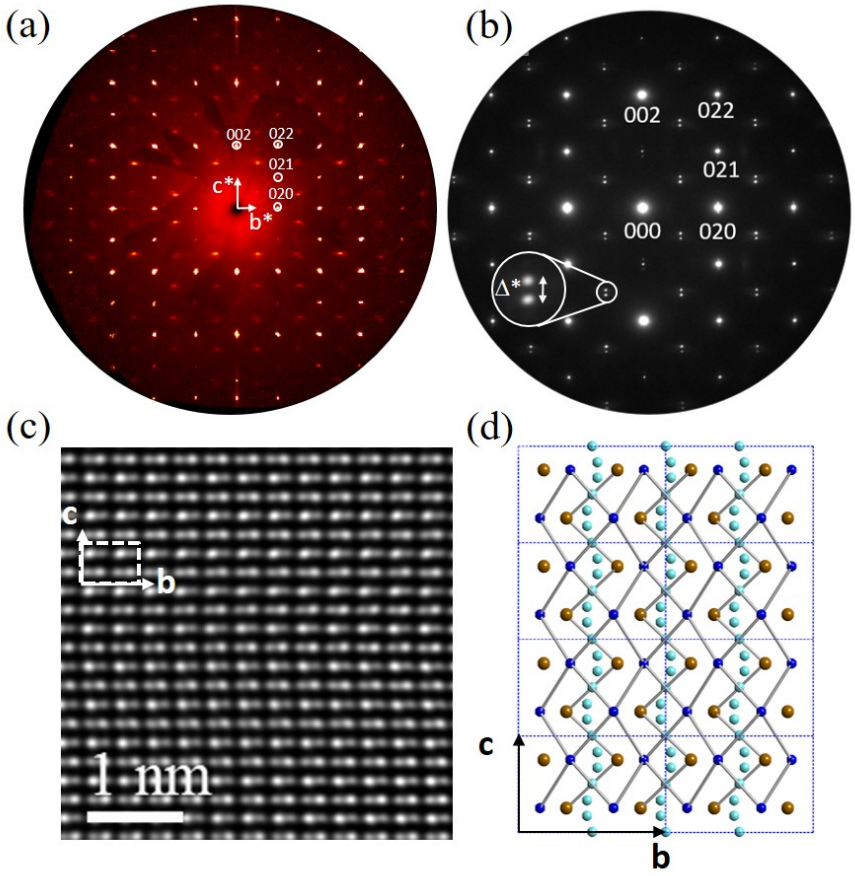

Figure 2: (a) (0kl) precession map obtained by single crystal X-ray diffraction showing the main reflections associated to the orthorhombic lattice plus additional splitted spots. (b) SAED pattern along the [100] zone axis, showing the main and superlattice reflections that are splitted by Δ^* along c*. (c) HAADF-STEM image of the structure with [100] incidence and (d) the corresponding projection of the crystal structure of the η phase according to the model by Burkhardt *et al.* [9]. The white rectangle in (c) shows the orthorhombic projected unit cell.

3.2 Ordered structural models for bulk Al_5Fe_2

The Al_5Fe_2 atomic structure consists of a rigid framework of pentagonal antiprims ($Al_4^{(8g)}Fe^{(4c)}$) extending along the [100] direction, connected by side edges and containing chains of fractionally occupied Al sites [9]. The stability of this phase, also identified as $Al_{2+\delta}Fe$, is strongly influenced by the precise atomic composition (δ), controlled by the filling of the Al-channels

in between the pentagonal antiprisms. It is investigated here through the formation enthalpies (ΔH_f), computed for several representatives of the Al_5Fe_2 compound, starting from the data published by Burkhardt *et al.* [9] (elemental $1 \times 1 \times 1$ cell with composition $Al_{2.5}Fe$) and considering $Al_{2+\delta}Fe$ compositions with $\delta = \frac{3}{5}$ ($1\times1\times5$ supercell), $\delta = \frac{2}{3}$ ($1\times1\times3$ supercell), $\delta = \frac{3}{4}$ ($1 \times 1 \times 2$ supercell). Of course, there are several possibilities to locate the Al atoms on the Al channel sites, leading to small variations in total energy calculations ($\Delta E < 7$ meV/at). Here we choose one of these possibilities while respecting the constraint on average interatomic distances between Al channel sites. Total energy calculations were performed with cell shapes and volumes kept fixed during the structural optimizations, to focus on the electronic effects induced by the filling of the weakly ordered Al-channels on the Al_5Fe_2 stability.

Total energy calculations were also performed using the structures of the recently published η'-Al_8Fe_3 [6], η"-Al_5Fe_2 (oP194) [11] and η"'-Al_5Fe_2 (oP314) [11] compounds. The crystal cells were fully relaxed, leading to theoretical structures in good agreement with the experimental data (relative errors less than 1%, Tab. 2).

Compd.	% Al (δ)	a (Å)	b (Å)	c (Å)	β (^{o})	ΔH_f (eV/at)
η'-Al_8Fe_3	72.72 ($\frac{2}{3}$)	11.28	6.40	8.63	104.58	-0.3388
		11.36[6]	6.42[6]	8.68[6]	104.25[6]	
η"-Al_5Fe_2	73.20 (0.73)	54.38	6.40	7.65		-0.3307
		54.76[11]	6.42[11]	7.65[11]		
η"'-Al_5Fe_2	73.25 (0.74)	87.98	6.40	7.65		-0.3288
		88.43[11]	6.42[11]	7.65[11]		

Table 2: Relaxed lattice parameters and formation enthalpies of the long-range ordered structures η'-Al_8Fe_3, η"-Al_5Fe_2, and η"'-Al_5Fe_2.

Formation enthalpies were computed for all considered structures. They are plotted in Fig. 3, as a function of the number of electrons per Fe atom ($\frac{3\times N_{Al}+8\times N_{Fe}}{N_{Fe}}$). The most stable structure for the Al_2Fe composition is the tI6 phase, with a formation enthalpy of -0.356 eV/at, as reported previously [13]. The stabilities within the $Al_{2+\delta}Fe$ series reach an extremum for the compound with four Al atoms in three c repeat units per Al-channel, i.e. $Al_{2.67}Fe$, in agreement with the $18 - n$ electron rule, as already mentioned [15]. The corresponding formation enthalpy, calculated to be -0.329 eV/at., is in good agreement with the literature (ΔH_f^{exp} = -0.288 eV/at at 300 K [36], ΔH_f^{calc} = -0.349 eV/at [13]). With this composition fixed, further stabilization occurs through the deformation of the crystal cell, from orthorhombic $Al_{2.67}Fe$ to monoclinic η'-Al_8Fe_3 (Tab. 2). The volumes of the two previous crystal cells are almost the same (622.0 Å^3 and 622.7 Å^3

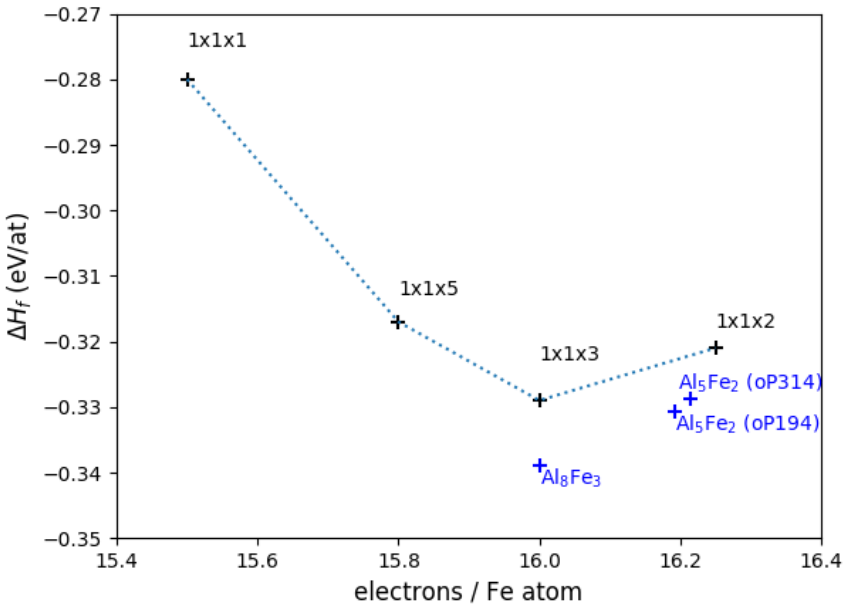

Figure 3: Formation enthalpies of selected ordered compounds with compositions along the Al_2Fe-Al_3Fe range. Several $1 \times 1 \times n$ supercells ($n \in \{1, 2, 3, 5\}$) were considered, starting from the structure proposed by Burkhardt *et al.* [9]. The long-range ordered structures (η'-Al_8Fe_3, η"-Al_5Fe_2 (oP194) and η"'-Al_5Fe_2 (oP314)) [6, 11] were considered as well.

respectively), but the formation enthalpy of η'-Al_8Fe_3 (-0.3388 eV/at.) is much lower than the one of orthorhombic $Al_{2.67}Fe$ (-0.3293 eV/at). Finally, the formation enthalpies of the commensurate long-period superstructures (η"-Al_5Fe_2 and η"'-Al_5Fe_2) are slightly higher than the one of η'-Al_8Fe_3. This is consistent with the higher number of electrons per Fe atoms in these systems. Those two structures are however more stable than the $Al_{2.75}Fe$ structure ($1 \times 1 \times 2$ supercell).

Electronic factors strongly contribute to the stability of complex intermetallic compounds. The electronic structures of the long-range ordered compounds (η'-Al_8Fe_3, η"-Al_5Fe_2 and η"'-Al_5Fe_2) are characterized by a *sp*-band at low energy and a Fe-*d* band in the region [-4 eV; 0 eV] (Fig. 4). A deep pseudo-gap (minimum in the DOS) is noticeable close to the Fermi energy, which likely contributes to stabilize the structure. While the Al_8Fe_3 is calculated to be non-magnetic, the two other compounds present a small magnetic moment (0.29 μ_B/Fe and 0.10 μ_B/Fe, on average, for the η" and η"' compounds, respectively), consistent with the DOS calculations. Further investigation of the Al-Al, Fe-Fe and Al-Fe hybridizations within the

framework of pentagonal antisprisms, as well as between the Al distorded chain and the framework, has been achieved with the $1 \times 1 \times 3$ model system (Fig. 5). The Fe-Fe interactions show a clear bonding character involving *d*-states near -2 eV, and a slight antibonding contribution close to the Fermi energy, leading to rather weak ICOHPs (-0.21 eV/bond, $r_{\mathrm{Fe-Fe}} = 2.95$ Å). The Al-Al interactions between *sp*-states reveal a strong bonding character, the strongest bonds (largest absolute values of ICOHPs) being found among Al-Al bonds of the framework ($d_{\mathrm{Al-Al}} \approx 2.6$ Å, ICOHP≈ -2.5 eV/bond). The Fe-Al ICOHPs ($d_{\mathrm{Fe-Al}} \approx 2.3$ Å) are smaller (≈-1.75 eV/bond), as well as the interactions between Al atoms of the distorded chain (-0.87 eV/bond on average), due to the filling of antibonding states in the latter case.

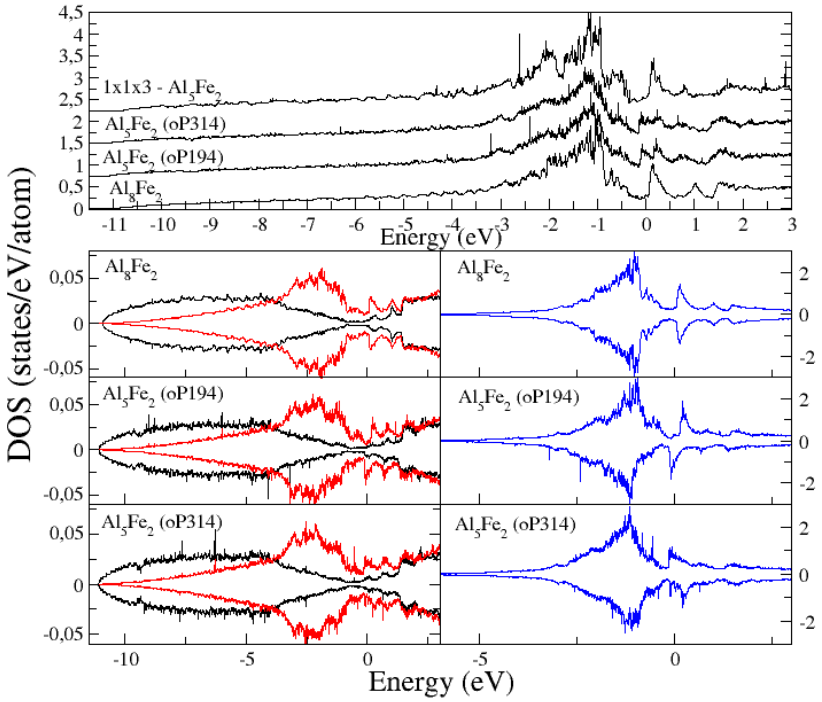

Figure 4: Density of states of Al_8Fe_3 and long-range ordered η" and η"' Al_5Fe_2 structures. The total DOS (upper panel), as well as the contributions from Al *sp*-states (left column, black = *s*-states, red = *p*-states) and Fe *d*-states (right column, blue) are plotted as a function of the binding energy. The Fermi level is set to zero.

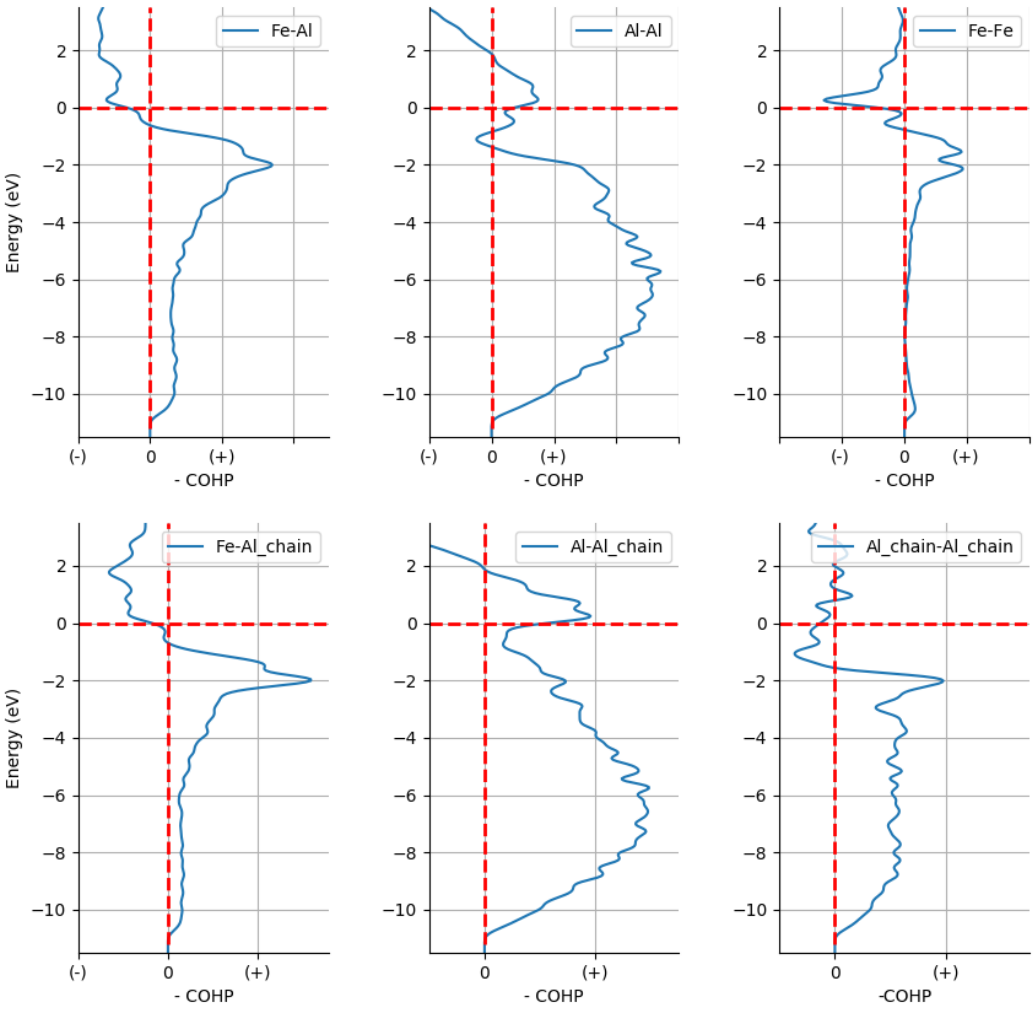

Figure 5: Average COHPs for Al-Al, Al-Fe and Fe-Fe bonds, as well as for interactions between the Al-chain and the framework, calculated with the 1x1x3 bulk model.

3.3 $Al_5Fe_2(001)$

3.3.1 Experimental results

The (001) surface has been prepared by sputtering and annealing within a temperature range extending from 843 K up to 1033 K. The near-surface composition has been measured by XPS as a function of the take-off angle of the photoemitted electrons (between 25 to 75° measured with respect to the surface plane) to vary the surface sensitivity of the measurements. The composition is derived from the area of the Al *2p* and Fe *2p* core levels after subtracting the Mg Kα satellites and a Shirley background. The area under the core levels have been corrected by a normalization coefficient taking into account the photoionization cross section, the photoelectron inelastic mean free path and the analyzer transmission function as described in [37]. The Al content ranges between 80 and 85 $\pm$ 5 at.% as seen in Fig. 6(a). It is in any case larger than what is expected from the bulk concentration by about 10 %. It suggests an Al enrichment in the near surface region compared to the bulk concentration. Near-surface concentrations measured by XPS reported for several Al-transition metal systems also indicated an Al content larger than the bulk nominal composition [37, 38]. The deviation was usually interpreted by the fact that the surface terminates at Al-rich plane of the bulk structure and does not necessarily reflect a surface segregation phenomenon. This is supported by the fact that the near-surface concentration measured by XPS was constant over the depth sampled in angle-resolved XPS measurements. In the present case, a slight increase of the Al content is observed at the lowest take-off angles.

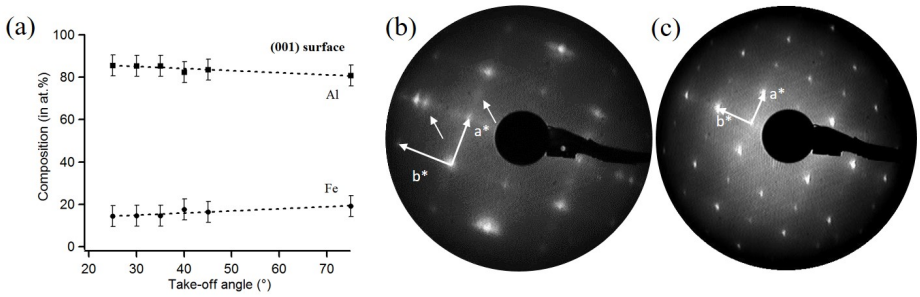

Figure 6: (a) Variation of the chemical concentration at the $Al_5Fe_2(001)$ surface as a function of the photoelectrons take-off angle. The dashed lines are linear fits to the data points. A slight Al enrichment is observed at low take-off angles (*i.e.* high surface sensitivity). (b,c) LEED patterns of the $Al_5Fe_2(001)$ surface recorded at 37 eV (b) and 88 eV (c). The surface was annealed at 900 K. The arrows in panel (b) indicates diffuse intensity at $a^*/2$ positions and facet spots moving along b^*.

Typical LEED patterns of the surface are shown in Fig. 6. It shows a (1x1) structure independently of the annealing temperature used for surface preparation. The reciprocal space has been calibrated using a LEED pattern of a reference sample recorded under similar conditions and the measured a and b parameters are in agreement with the bulk values. At low electron energies and depending on the thermal history of the sample, some weak spots were also observed at $a^*/2$ positions (Fig. 6(b)) as well as other spots moving along b^* when the energy is varied, characteristic of surface faceting. These additional features in the LEED pattern were not observed systematically, even for similar surface preparation conditions.

The (001) surface was also investigated by STM after sputter-annealing cycles at various temperatures. The surface was always rough, with some clustered areas, areas of step-bunching and some areas presenting a step-terrace morphology. A step height of 4.2 Å$\sim c$ was most frequently measured. Additional 2.1 Å$\sim c/2$ steps were also observed occasionally, associated with very narrow terraces appearing between two larger ones. Adatoms or groups of adatoms were always present on the terraces making it difficult to obtain atomically resolved STM images. An example is shown in Fig. 7. Atomic rows extending along b can be seen. The unit cell dimensions measured from STM images are equal to 6.4 $\pm$ 0.2 Å along the rows (b) and 7.6 $\pm$ 0.3 Å perpendicular to them (a). There is weak pairing of the atomic rows observed in the STM image (see Fig. 7b). It is also reflected by a weak spot in the fast-Fourier transform (FFT) of the image. This is consistent with the weak diffuse $a^*/2$ spots in the LEED pattern. In addition, the STM contrast along b is not regular and the surface contains many defects which can explain the diffuse intensities in the LEED patterns (Fig. 6(a)).

The pairing of the atomic rows in the (001) surface plane is not expected from the bulk structure. In addition, dense planes along the c direction are located at c/4 and 3c/4 and have the same structure. It is thus expected that both planes should appear as surface termination, leading to a preferred $c/2$ step height - in contradiction with the observation.

After a number of sputtering and annealing cycles, the surface which was initially mirror like developed a milky appearance. The LEED pattern was essentially unchanged but the surface became more and more rough and clustered as observed by STM. The sample was then removed from the UHV chamber. Optical micrography as well as scanning electron microscopy revealed the formation of pits correlated with the surface milkiness. Some small precipitates might also have formed according to SEM images, but are too small to allow for their chemical identification by EDS. The average chemical composition measured by EDS was unchanged compared to the bulk one. One possible reason for this macroscopic surface modification might be the preferential diffusion of loosely bounded Al along the channels in the [001] direction as documented in Ref. [13, 14] which may lead to an accumulation of aluminum at the surface upon annealing cycles. If excess

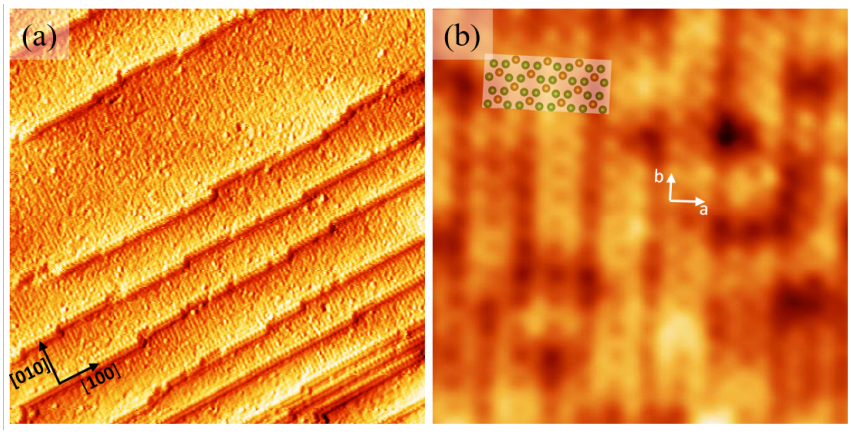

Figure 7: STM images of the $Al_5Fe_2(001)$ surface after annealing at 953 K. (a) 70x70 nm^2, V_b= - 2V. (b). 10x10 nm^2, V_b= - 2V. A model of the bulk c/4 layer containing Al(1) atoms (green) and Fe atoms (brown) has been superimposed to the experimental image. The sample has been rotated in (b) compared to (a).

aluminum diffuse and condense at the (001) surface, it might form aluminum mounds or contribute to the formation of Al-rich precipitates (monoclinic $Al_{13}Fe_4$ according to the phase diagram), leading to an increased surface roughness. However, XPS measurements performed on the milky surface did not revealed any significant increase of the Al content compared to that of the mirror like surface. Al evaporation is not expected either as its vapor pressure is still extremely low even at the highest annealing temperature used. The surface could not be investigated further due to this problem.

3.3.2 Theoretical results

To get further insight into the (001) surface structure, we performed DFT calculations using a 12-layer thick slab built by bulk truncation. We took the orthorhombic $Al_{2.67}Fe$ bulk structure, as an approximant structure of the η"-Al_5Fe_2 phase. The termination plane contains a pentagonal motif, made of four Al and one Fe atoms located in the rigid framework of pentagonal antiprisms extending along the [001] direction. Atomic relaxations lead to a clear rumpling at the surface ($\approx$ 0.17 Å), Fe and Al atoms lying slightly below and above the topmost plane average position, respectively. This is in agreement with the finding that Fe is not likely at the Al(100) surface [39]. The corresponding STM image simulated using the previous surface model leads to a bright squared-like network, resulting from the contribution of all topmost surface atoms (Fig. 8) and leading to a poor agreement with the

experimental image.

An additional surface model has been built, by removing one surface Fe atom in the surface cell. Depending on the chemical potentials, the formation of a Fe surface vacancy can be exothermic (ΔH_f(vacFe) = -0.60 eV per Fe vacancy if $\mu_{Al} = \mu_{Al}^{fcc}$) or endothermic ($\Delta H_f$(vacFe) = 0.60 eV per Fe vacancy if $\mu_{Fe} = \mu_{Fe}^{bcc}$). The STM image simulations, based on this model, lead to a better agreement with the experimental images (Fig. 8). It suggests that the observed pairing of atomic rows in the (001) surface plane is due to missing rows of Fe atoms, leading to the formation of lines with darker contrast extending along *b*. Note that in the model with Fe vacancies, one of two equivalent Fe atomic positions per surface unit cell has been removed arbitrarily. If one select the other atomic position for Fe vacancies, the line with darker contrast in simulated STM image will shift by $a/2$. Such a shift can actually be seen at the bottom left corner of the experimental image shown in Fig. 7(b). The formation of Fe surface vacancies is consistent with the slight Al-enrichment at low take-off angle measured by XPS.

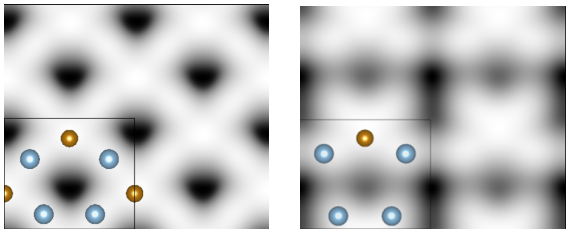

Bulk terminated Surface Fe vacancy

Figure 8: Simulated STM images of Al_5Fe_2(001).

3.4 $Al_5Fe_2(100)$

3.4.1 Experimental results

The (100) surface has been prepared by sputtering and annealing in a temperature range from 793 K to 948 K. The near-surface composition has been measured by XPS as a function of the take-off angle and is shown in Fig. 9(a). The Al content amounts to 82 ± 5 at.%, which is again larger than the bulk concentration by about 10 %. The Al content does not increase with the surface sensitivity contrary to the case of the (001) surface.

Typical LEED patterns of the (100) surface obtained after annealing at 810 K are shown in Fig. 9(b,c) for two different primary beam energies. The most intense spots are the (1x1) spots with surface unit mesh $b = 6.4 \pm 0.2$ Å and $c = 4.2 \pm 0.1$ Å matching the expected bulk values. Additional spots are observed forming an average (2x2) superlattice where all spots having integer coordinates along c* are missing. Furthermore, a splitting of the spots having a half-integer coordinates both along b^* and c^* is observed. The two split spots have different intensities which vary also differently with the electron beam energy. The split distance between these two spots is the same as the one measured in SAED pattern ($\Delta^* \sim 0.086$ c*). The two sets of spots correspond to real space distances of 9.3 and 7.5 Å along c, i.e. $\sim$ 2c ± 10%. The LEED patterns are thus consistent with a doubling of the unit cell along the b direction and a modulation with an average $2c$ periodicity along the direction of the Al channels. The magnitude of the modulation vector along c^* is $q \sim (1/2 - \Delta^*/2) \sim 0.46c^*$, similar to the value reported in [11] for the bulk.

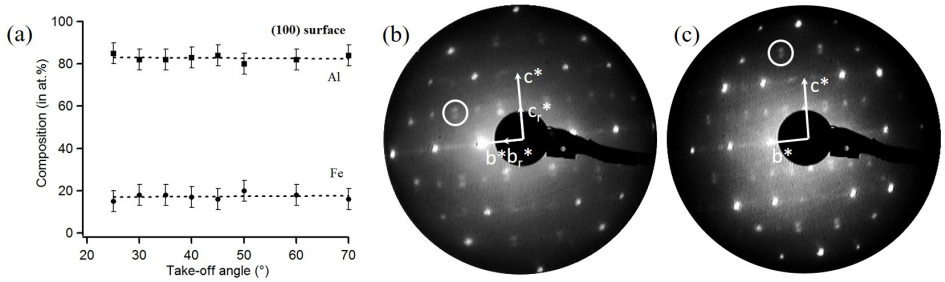

Figure 9: (a) Variation of the chemical concentration at the $Al_5Fe_2(100)$ surface as a function of the photoelectrons take-off angle. The dashed lines are linear fits to the data points. (b,c) LEED patterns of the $Al_5Fe_2(100)$ surface after annealing at 810 K. (b) 59 eV and (c) 80 eV. Split spots correspond to real space distances of 9.3 ± 0.3 Å and 7.5 ± 0.2 Å corresponding to 2c± 10%.

STM images of the surface show large terraces separated by a unique

step height of 3.8 Å$\sim a/2$ (see Fig.10a). It is frequent to observe elongated terrace stripes along the c direction at the end of which mounds can be seen as shown in Fig.10b. An hypothesis is that these mounds are due to an accumulation of Al easily diffusing along the channels and emerging at step edges. High-resolution STM images of the terrace structure (Fig.10c) show an approximate rectangular centered unit cell with dimensions b_R=12.6 ± 0.2 Å and c_R=8.5 ± 0.2 Å, consistent with the observed average (2x2) LEED pattern. The fast-Fourier transform (FFT) of the STM image is shown in Fig.10d. In addition to the bright and sharp (1,0) spots, some more diffuse and less intense spots are observed at ∼(1/2,1/2) position. These spots are splitted along c^*, with a split distance equal to 0.12 ± 0.03c^*, slightly larger than that deduced from LEED and SAED patterns. Such spot splitting can already be observed in the fast-Fourier transform of individual atomic rows along c. These spots in the FFT correspond to real space distances equal to 9.6 ± 0.2 Å and 7.5 ± 0.2 Å. It means that the bright protrusions seen in STM images are not exactly periodically spaced along c but the spacing between adjacent protrusions takes one of these two values in a non periodic way, as verified from line profiles of STM images taken along c. From the relative intensity of the two split spots, the spacing of 9.6 Å appears more frequently than that of 7.5 Å. This incommensurate modulation of the STM contrast cannot be explained on the basis of the orthorhombic *Cmcm* space group and could be linked with the observation of the η" superstructure observed in the bulk. However, the length scale of the modulation of the STM contrast (∼2c) is much larger than the average interatomic distances between Al channel sites (∼2.8 Å).

3.4.2 Theoretical results

Surface energies

To get further insight into the origin of the STM contrast and the surface structure, we performed DFT calculations for several possible slab models, built from the Burkhardt bulk structure with 3 Al atoms per 2c units per channel, therefore with composition $Al_{5.5}Fe_2$. Along the [100] direction, the bulk structure consists in a pile of two types of planes: a flat plane containing alternating Fe- and Al-rows (Al-channels) along the [001] direction, and a pure Al puckered plane, made of Al atoms from the rigid network. Two terminations are obtained by bulk truncation : a flat termination ($F^{Al,Fe}$) and an Al-pure puckered termination (P^{Al}). Two additional models are obtained by removing topmost Al atoms in the P^{Al} model ($^{vac}P^{Al}$) or topmost Fe atoms in the $F^{Al,Fe}$ model (F^{Al}). Side views of the models are shown in Fig. 11.

The corresponding relative surface energies are plotted in Fig. 12. The $F^{Al,Fe}$ model was chosen as a reference system. Negative values of relative surface energies then correspond to more stable models than the $F^{Al,Fe}$ one.

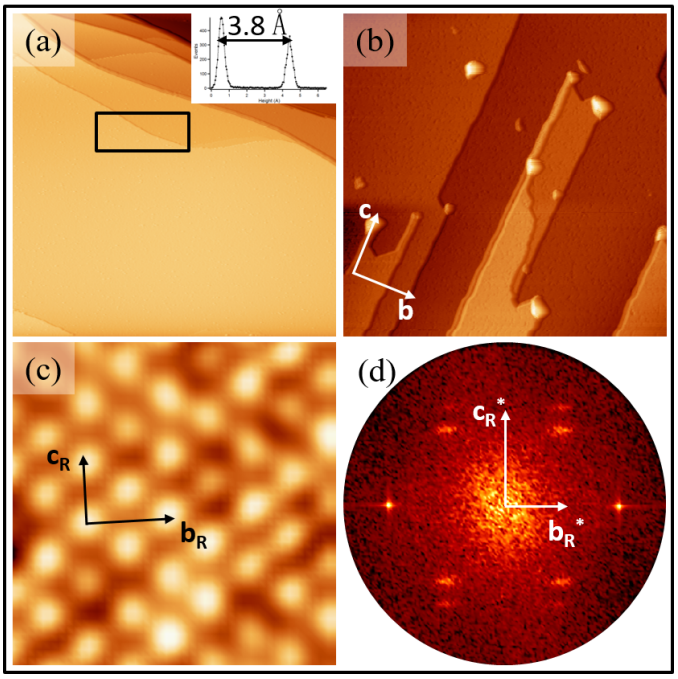

Figure 10: STM images of the $Al_5Fe_2(100)$ surface after annealing at 953 K. (a) 1x1 μm^2, V_b= - 2V. The inset is an height histogram of the rectangular area outlined in the image, showing a step height of 3.8 Å. (b) 200x200 nm^2, V_b= - 2V. (c). 5x5 nm^2, V_b= - 2V. The lattice vectors of the approximate centered rectangular unit cell are shown. (d) FFT of an STM image showing spot splitting.

Truncating the bulk structure at the flat plane is unlikely: $\gamma_{100}^{F^{Al,Fe}} > \gamma_{100}^{P^{Al}}$. This is attributed to the presence of surface Fe atoms, i.e. the metal with the highest surface energy ($\gamma_{Al(111)}$ = 0.05 eV/Å^2, $\gamma_{Fe(110)}$ = 0.15 eV/Å^2 [40]), in the $F^{Al,Fe}$ model. Removing the topmost Fe surface atoms of $F^{Al,Fe}$ also leads to a stabilization in a large range of chemical potentials, in the Al-rich region (see the surface energies of $F^{Al,Fe}$ and F^{Al} in Fig. 12).

Starting from the P^{Al} model, the formation of Al surface vacancies is thermodynamically favorable: the ${}^{vac}P^{Al}$ model presents the lowest surface energy in the full range of allowed chemical potentials. The reason lies in the strong bond, identified by pCOHP calculations, between topmost Al atoms in P^{Al} and Fe atoms positioned in the flat plane located above (but removed here to build the surface). This bond is stronger than the one with Fe atoms located in the same plane or below. In contrast, topmost Al surface atoms in ${}^{vac}P^{Al}$ are more strongly bonded to Fe atoms located in the subsurface plane than to atoms removed above the surface.

Since a (2x2) reconstruction has been identified by LEED, we built additional models by implementing Al vacancies, to obtain a reconstructed 2×2 surface cell. The models are labeled according to the number of Al vacancies: $F^{Al,Fe}_{4vac}$ (from $F^{Al,Fe}$), F^{Al}_{4vac} (from F^{Al}), ${}^{vac}P^{Al}_{6vac}$ (from ${}^{vac}P^{Al}$), P^{Al}_{2vac} and P^{Al}_{6vac} (from P^{Al}). The presence of Al vacancies in the Al-channel at the surface lead to a rather high increase of the surface energy ($\gamma^{F^{Al,Fe}_{4vac}}_{100} > \gamma^{F^{Al,Fe}}_{100}$), demonstrating the quite strong interaction between the Al atoms located in the Al-channels and the Fe atoms of the rigid framework, already identified by pCOHP calculations. Similarly, the presence of additional Al vacancies in the ${}^{vac}P^{Al}$ model is not favorable ($\gamma^{{}^{vac}P^{Al}_{6vac}}_{100} > \gamma^{F^{Al,Fe}}_{100}$), again because the surface Al atoms in ${}^{vac}P^{Al}$ are quite strongly bound to the Fe atoms located in the atomic plane below. Since we expect that the observed 2×2 reconstruction occurs to stabilize the surface, these two models are not considered in the following.

In contrast to what was described in the previous paragraph, surface Al vacancies stabilizes the F^{Al} and P^{Al} models, in the Fe-rich limit (F^{Al}_{6vac}, F^{Al}_{4vac}). In the Al-rich limit, the F^{Al} and P^{Al} models, and their derivatives, present the lowest relative surface energy calculated so far ($\simeq$ -1.2 J/m^2). In the following, the STM images simulated using these stable surface models are compared to the experimental observations.

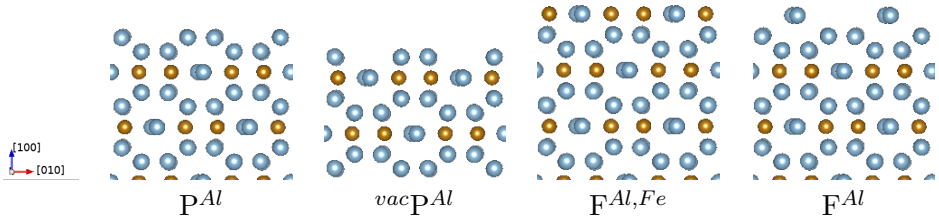

Figure 11: Side views of several surface models considered in this work.

Simulations of STM images have been performed for all models considered so far (Fig. 13). In most cases, the bright contrast is attributed to protruding Al atoms. Examples are the bright lines of models F^{Al} and $F^{Al,Fe}$, attributed to the Al-chains preserved at the surface. Surface Fe atoms usually do not induce a bright contrast : they relax inwards and are located

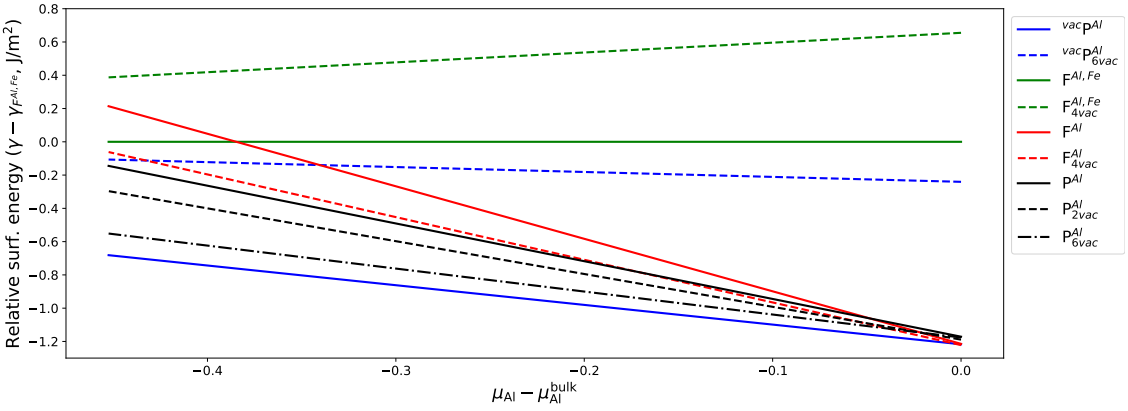

Figure 12: Surface energies of the different models considered in this study.

slightly below the mean position of the topmost plane. All (1x1) models, as well as model P^{Al}_{2vac}, fail to reproduce the approximate (2x2) rectangular centered unit cell observed experimentally.

The simulated images of the four remaining models (P^{Al}_{6vac}, $^{vac}P^{Al}_{6vac}$, $F^{Al,Fe}_{4vac}$, F^{Al}_{4vac}) show a (2x2) centered rectangular motif, the best agreement with the experimental image being obtained with the P^{Al}_{6vac} model. This model is also one of the most stable models. Due to the need of periodic boundary conditions, the superstructure considered here is necessarily periodic, but one can easily imagine to reproduce the more complex modulation observed experimentally by modifying slightly the location of the protruding Al atoms. There are 28 possible different configurations when removing six over eight crystallographically equivalent Al topmost surface atoms (P^{Al}_{6vac} model). Here we choose one of these possibilities. Further investigations are required to assess the chemical processes leading to this specific surface structure.

4 Conclusions

A single crystal of the Al_5Fe_2 compound has been grown by the Czochralski method. Although the powder X-ray diffraction pattern could be indexed as the orthorhombic η structure with *Cmcm* space group, single crystal X-ray diffraction and transmission electron microscopy experiments indicated that the crystal has the structure of the low temperature polymorph η" phase which is induced by a long-range ordering of the Al channel atoms. Formation enthalpy calculated for a number of superlattices based on the η structure indicates an optimized structure for 4 Al atoms in 3 c units per channel, thus fulfilling the (18-n) electron rule. The bonding analysis reveal

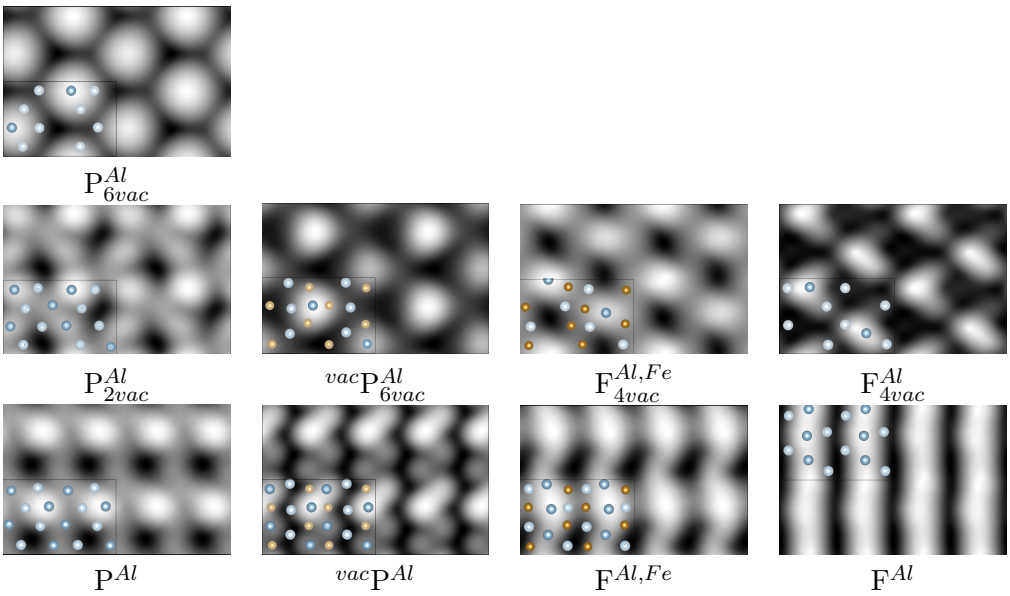

Figure 13: Simulated STM images of $Al_5Fe_2(100)$. See text for details about the surface models used for the calculations.

strong bonding character within the framework of pentagonal antiprisms and weaker interactions between Al channel atoms and the framework. Both the (001) and (100) surfaces of this compound have been investigated experimentally and theoretically. The (001) surface is perpendicular to the channel's direction. The LEED and STM results are consistent with a bulk terminated surface but additional diffuse intensity in the LEED patterns and high-resolution STM images indicate a pairing of the atomic rows which is not a bulk feature. Calculations suggest that this is due to the formation of missing rows of Fe in the bulk terminated surface. The (100) surface is parallel to the channel's directions. The LEED and STM results show evidences of a superstructure based on the orthorhombic primitive lattice. The superstructure observed at the surface manifests has an approximate (2x2) reconstruction with a rectangular centered unit cell. However split spots in LEED pattern reveal a more complex modulated structure in agreement with the η" bulk structure. Similar splitted spots are also observed in the FFT of STM images. Several surface models were constructed by bulk truncation, including surface models with Fe and Al surface vacancies. The surface energies of these models have been compared and STM images have been calculated from the electronic structure. It is concluded that the presence of Fe atoms at the surface is unlikely. Results suggest that the observed surface structure can be explained by bulk truncation at Al layers preserving the framework of pentagonal antiprisms, the presence of Al surface vacancies strongly stabilizing the ideal bulk truncated model, and leading to a good

agreement with the experimental STM images. These models are periodic by construction and cannot reproduce the observed incommensurate modulation. Further investigations are required to relate such surface ordering with the one of the Al channel sites.

5 Acknowledgments

This work was supported by the Lorraine Region and the European Integrated Centre for the Development of New Metallic Alloys and Compounds ECmetAC. It benefited French-Slovene collaboration established under the Push-Pull Alloys and Complex Compounds (PACS2) Joint Open Laboratory. E.G. acknowledges financial support through the COMETE project (COnception in silico de Matériaux pour l'EnvironnemenT et l'Energie) cofunded by the European Union under the program "FEDER-FSE Lorraine et Massif des Vosges 2014-2020". High Performance Computing resources were provided by GENCI under the allocation 99642, IDRIS under the allocation 2015096339 as well as the EXPLOR center hosted by the Université de Lorraine (allocation 2017M4XXX0108). We also acknowledge the funding of our research activities by the Slovenian Research Agency through the program P2-0084.

References

[1] R. W. Richards, R. D. Jones, P.D. Clements, and H. Clarke. Metallurgy of continuous hot dip aluminising. *International Materials Reviews*, 39:191–212, 1994.

[2] N. Takata, M. Nishimoto, S. Kobayashi, and M. Takeyama. Crystallography of Fe_2Al_5 phase at the interface between solid Fe and liquid Al. *Intermetallics*, 67:1–11, 2015.

[3] K. Han, I. Ohnuma, and R. Kainuma. Experimental determination of phase equilibria of Al-rich portion in the al-fe binary system. *Journal of Alloys and Compounds*, 668:97–106, 2016.

[4] X. Li, A. Scherf, M. Heilmaier, and F. Stein. The al-rich part of the fe-al phase diagram. *Journal of Phase Equilibria and Diffusion*, 37:162–173, 2016.

[5] N.L. Okamoto, J. Okumura, M. Higashi, and H. Inui. Crystal structure of η'-Fe_3Al_8; low-temperature phase of η-Fe_2Al_5 accompanied by an ordered arrangement of al atoms of full occupancy in the c-axis chain sites. *Acta Materialia*, 129:290–299, 2017.

[6] H. Becker, L. Amirkhanyan, J. Kortus, and A. Leineweber. Powder-x-ray diffraction analysis of the crystal structure of the η'-Al_8Fe_3 (η'-$Al_{2.67}Fe$) phase. *Journal of Alloys and Compounds*, 721:691– 696, 2017.

[7] K. Schubert, U. Rösler, M. Kluge, K. Anderko, and L. Härle. Kristallographische ergebnisse an phasen mit durchdringungsbindung. *Naturwissenschaften*, 40:437, 1953.

[8] M. Ellner and J. Mayer. X-ray and electron diffraction investigations of the liquid-quenched Fe_2Al_5. *Scripta Metallurgica et Materialia*, 26:501–504, 1992.

[9] U. Burkhardt, Y. Grin, M. Ellner, and K. Peters. Structure refinement of the iron-aluminium phase with the approximate composition Al_5Fe_2. *Acta Crystallographica*, B50:313–316, 1994.

[10] F. Stein, G. Sauthoff, and M. Palm. Phases and phase equilibria in the Fe-Al-Zr system. *Zeitschrift für Metallkunde*, 95(6):469–485, 2004.

[11] H. Becker and A. Leineweber. Atomic channel occupation in disordered η-Al_5Fe_2 and in two of its low-temperatures phases, η" and η"'. *Intermetallics*, 93:251– 262, 2018.

[12] N.L. Okamoto, M. Higashi, and H. Inui. Crystal structure of η"-Fe_3Al_{7+x} determined by single-crystal synchrotron x-ray diffraction combined with scanning transmission electron microscopy. *Science and Technology of Advanced Materials*, 20:543–556, 2019.

[13] M. Mihalkovic and M. Widom. Structure and stability of Al_2Fe and Al_5Fe_2: First-principles total energy and phonon calculations. *Physical Review B*, 85:014113, 2012.

[14] R. Sakidja, J.H. Perepezko, and P. Calhoun. Synthesis, thermodynamic stability and diffusion mechanism of Al_5Fe_2-based coatings. *Oxidation of Metals*, 81:167–177, 2014.

[15] A. I. Vinokur, K. P. Hilleke, and D. C. Fredrickson. Principles of weakly ordered domains in intermetallics: the cooperative effects of atomic packing and electronics in Fe_2Al_5. *Acta Cryst.*, A75:297–306, 2019.

[16] I. Horcas, R. Fernandez, J. M. Gomez-Rodriguez, J. Colchero, J. Gomez-Herrero, and A. M. Baro. Wsxm: A software for scanning probe microscopy and a tool for nanotechnology. *Review of Scientific Instruments*, 78:013705, 2007.

[17] G. Kresse and J. Hafner. Ab initio molecular dynamics for liquid metals. *Phys. Rev. B*, 47:558–561, 1993.

[18] G. Kresse and J. Hafner. Ab initio molecular-dynamics simulation of the liquid-metal-amorphous-semiconductor transition in germanium. *Phys. Rev. B*, 49:14251–14269, 1994.

[19] G. Kresse and J. Furthmüller. Efficient iterative schemes for ab initio total-energy calculations using a plane-wave basis set. *Phys. Rev. B*, 54:11169 – 11186, 1996.

[20] G. Kresse and J. Furthmüller. Efficiency of ab-initio total energy calculations for metals and semiconductors using a plane wave basis set. *Comput. Mater. Sci.*, 6:15–50, 1996.

[21] P. E. Blochl. Projector augmented-wave method. *Phys. Rev. B*, 50:17953–17979, 1994.

[22] G. Kresse and D. Joubert. From ultrasoft pseudopotentials to the projector augmented-wave method. *Phys. Rev. B*, 59:1758–1775, 1999.

[23] J. P. Perdew, K. Burke, and M. Ernzerhof. Generalized gradient approximation made simple. *Phys. Rev. Lett.*, 77:3865, 1996.

[24] J. P. Perdew, K. Burke, and M. Ernzerhof. Erratum: Generalized gradient approximation made simple. *Phys. Rev. Lett.*, 78:1396, 1997.

[25] K. Momma and F. Izumi. VESTA 3 for three-dimensional visualization of crystal, volumetric and morphology data. *J. Appl. Crystallogr.*, 44:1272–1276, 2011.

[26] R. Dronskowski and P. E. Blöchl. The original COHP definition. *J. Phys. Chem.*, 97:8617–8624, 1993.

[27] V. L. Deringer, A. L. Tchougréeff, and R. Dronskowski. Crystal orbital hamilton population (COHP) analysis as projected from plane-wave basis sets. *J.Phys.Chem. A*, 115:5461–5466, 2011.

[28] S. Maintz, V. L. Deringer, A. L. Tchougréeff, and R. Dronskowski. The mathematical apparatus and the framework on which LOBSTER is built. *J. Comput. Chem.*, 34:2557–2567, 2013.

[29] S. Maintz, V. L. Deringer, A. L. Tchougreeff, and R. Dronskowski. Lobster: A tool to extract chemical bonding from plane-wave based dft. *J. Comput. Chem.*, 37:1030–1035, 2016.

[30] F. Bechstedt. *Principles of surface physics*. Springer, Berlin, 2003.

[31] F. Chiter, V. B. Nguyen, N. Tarrat, M. Benoit, H. Tang, and C. Lacaze-Dufaure. Effect of van der Waals corrections on DFT-computed metallic surface properties. *Mater. Res. Express*, 3:046501, 2016.

[32] A. S. Cooper. Precise Lattice Constants of Germanium, Aluminum, Gallium Arsenide, Uranium, Sulphur, Quartz and Sapphire. *Acta Crystallogr.*, 15:578–582, 1962.

[33] C. Kittel. *Introduction to Solid State Physics*. John Wiley & Sons, USA, 7 edition, 1996.

[34] P. Janthon, S. Luo, S. M. Kozlov, Francesc Vines, J. Limtrakul, D. G. Truhlar, and F. Illas. Bulk properties of transition metals: A challenge for the design of universal density functionals. *J. Chem. Theory Comput.*, 10:3832–3839, 2014.

[35] Z.S. Basinski, W. Hume-Rothery, and A.L. Sutton. The lattice expansion of iron. *Proceedings of the Royal Society of London, Series A: Mathematical and Physical Sciences*, 229:459–467, 1955.

[36] R. Hultgren, P. D. Desai, D. T. Hawkins, M. Gleiser, and K. K. Kelley. *Selected Values of the Thermodynamic Properties of Binary Alloys*. ASM International, 1973.

[37] S. Alarcón-Villaseca, J. Ledieu, L. Serkovic-Loli, M.-C. de Weerd, P. Gille, V. Fournée, J.-M. Dubois, and É. Gaudry. Structural investigation of the (001) surface of the Al_9Co_2 complex metallic alloy. *J. Phys. Chem. C*, 115:14922–14932, 2011.

[38] M. Meier, J. Ledieu, M.C. de Weerd, Y.-T. Huang, G.J.P. Abreu, K. Pussi, R.D. Diehl, T. Mazet, V. Fournée, and É Gaudry. Interplay between bulk atomic clusters and surface structure in complex intermetallic compounds: The case study of the $Al_5Co_2(001)$ surface. *Phys. Rev. B*, 79:184201, 2009.

[39] D. Dubaux, É. Gaudry, M.C. de Weerd, S. Sturm, M. Podlogar, J. Ghanbaja, S. Migot, V. Fournée, M. Sicot, and J. Ledieu. Metastable Al-Fe intermetallic stabilised by epitaxial relationship. *submitted*.

[40] R. Tran, Z. Xu, B. Radhakrishnan, D. Winston, W. Sun, K.A. Persson, and S. Ping-Ong. Surface energies of elemental crystals. *Scientific Data*, 3:160080, 2016.